remote sensing

MDPI

Article

Improvement of GOCI-II Water Vapor Absorption Correction through Fusion with GK-2A/AMI Data

Kyeong-Sang Lee [1], Myung-Sook Park [1,2], Jong-Kuk Choi [1] and Jae-Hyun Ahn [1,*]

[1] Korea Institute of Ocean Science and Technology, Korea Ocean Satellite Center, Busan 49111, Republic of Korea
[2] National Aeronautics and Space Administration (NASA), Goddard Space Flight Center (GSFC), Greenbelt, MD 20771, USA
* Correspondence: brtnt@kiost.ac.kr; Tel.: +82-51-664-3161

Abstract: In remote sensing of the ocean color, in particular, in coarse-resolution global model simulations, atmospheric trace gases including water vapor are generally treated as auxiliary data, which create uncertainties in atmospheric correction. The second Korean geostationary satellite mission, Geo-Kompsat 2 (GK-2), is unique in combining visible and infrared observations from the second geostationary ocean color imager (GOCI-II) and the advanced meteorological imager (AMI) over Asia and the Pacific Ocean. In this study, we demonstrate that AMI total precipitable water (TPW) data to allow realistic water vapor absorption correction of GOCI-II color retrievals for the ocean. We assessed the uncertainties of two candidate TPW products for GOCI-II atmospheric correction using atmospheric sounding data, and then analyzed the sensitivity of four ocean-color products (remote sensing reflectance [R_{rs}], chlorophyll-a concentration [CHL], colored dissolved organic matter [CDOM], and total suspended sediment [TSS]) for GOCI-II water vapor transmittance correction using AMI and global model data. Differences between the TPW sources increased the mean absolute percentage error (MAPE) of R_{rs} from 2.97% to 6.43% in the blue to green bands, higher than the global climate observing system requirements (<5%) at 412 nm. By contrast, MAPE values of 3.53%, 6.18%, and 7.71% were increased to 6.63%, 13.53%, and 16.14% at high sun and sensor zenith angles for CHL, CDOM, and TSS, respectively. Uncertainty analysis provided similar results, indicating that AMI TPW produced approximately 3-fold lower error rates in ocean-color products than obtained using TPW values from the National Centers for Environmental Prediction. These results imply that AMI TPW can improve the accuracy and ability of GOCI-II ocean-color products to capture diurnal variability.

Keywords: second geostationary ocean color imager; advanced meteorological imager; total precipitable water; gaseous absorption correction; uncertainty analysis

check for updates

Citation: Lee, K.-S.; Park, M.-S.; Choi, J.-K.; Ahn, J.-H. Improvement of GOCI-II Water Vapor Absorption Correction through Fusion with GK-2A/AMI Data. *Remote Sens.* **2023**, *15*, 2124. https://doi.org/10.3390/rs15082124

Academic Editor: Manuel Antón

Received: 27 February 2023
Revised: 12 April 2023
Accepted: 15 April 2023
Published: 17 April 2023

Copyright: © 2023 by the authors. Licensee MDPI, Basel, Switzerland. This article is an open access article distributed under the terms and conditions of the Creative Commons Attribution (CC BY) license (https://creativecommons.org/licenses/by/4.0/).

1. Introduction

Remote sensing data of ocean color collected by satellites are used to construct various ocean environmental products such as chlorophyll-a concentration (CHL) [1–3], total suspended sediment (TSS) [4–6], and colored dissolved organic matter (CDOM) absorption [7–9]. Therefore, such data have been widely employed to improve efficiency and reduce the cost of coastal and open seas monitoring [10]. Ocean-color products are typically analyzed based on the inversion of radiative transfer theory using ocean reflectance spectra, e.g., remote sensing reflectance (R_{rs}) derived from satellite observations of top-of-atmosphere (TOA) radiance. However, TOA radiance includes R_{rs} at the sea surface along with atmospheric path reflectance, and light can be attenuated before reaching the satellite sensor due to scattering by air molecules and aerosols. Atmospheric path reflectance accounts for more than 90% of TOA observations, such that effective discrimination of a signal from the ocean surface remains challenging. To remove atmospheric effects from

TOA radiance observed by ocean-color sensors, the physical-based atmospheric correction algorithm consists of corrections for gas absorption, molecular scattering, aerosol scattering and absorption, bidirectional reflectance distribution, and turbid water [10]. This study focuses mainly on gas absorption correction, which corrects solar radiation absorbed by trace gases (e.g., ozone, water vapor, or nitrogen dioxide) in the sunlight path. Gas absorption directly affects TOA radiance measured by sensors; thus, a small error in gas absorption correction can cause nonnegligible error in atmospheric correction, and the impact on the R_{rs} of gas absorption correction differs among observation conditions [11]. Therefore, a realistic consideration of atmospheric gas absorption in atmospheric correction is necessary to enhance the quality of primary ocean-color products [12–16].

Atmosphere correction algorithms for ocean-color sensors typically use trace gas data from models and other satellites as ancillary data [17,18] because their different wavelength range makes it challenging to accurately estimate trace gas information. The accuracy of atmospheric correction is sensitive to gaseous absorption correction, which is applied directly to TOA reflectance [19–21]. Unlike ozone and nitrogen dioxide, water vapor absorption affects both the visible (VIS) and near-infrared (NIR) bands used to estimate aerosol reflectance for entire wavelengths. Negligible uncertainty in aerosol type determination for the NIR bands generally leads to significant uncertainty in the VIS bands [10].

The second geostationary ocean color imager (GOCI-II), the successor of the world's first geostationary ocean color imager (GOCI), has been operated by the Korea Ocean Satellite Center of Korea Institute of Ocean Science and Technology since February 2020 [22]. The unpreceded characteristic of GOCI-II is that it operates with its triplet sensors, advanced meteorological imager (AMI) [23], and geostationary environmental monitor spectrometer (GEMS) [24] on the same geostationary orbit (128.2°E over the equator). A unique operating system that simultaneously operates GOCI-II, GEMS, and AMI on the same orbit can enhance environmental monitoring capabilities. GOCI-II has moderate spatial (250 m at nadir) and spectral resolution (12 spectral bands from 380 to 865 nm) with unprecedented temporal resolution (10 daytime images per day), and observes the Northeast Asian Sea including the Korean Peninsula. Its main advantage is that it observes diurnal variation in ocean environments, including sediment variation within the tidal cycle and red tide migration [25]. Thus, more precise atmospheric correction is required for these data because there is less diurnal fluctuation than daily variation.

The GOCI-II atmospheric correction algorithm was developed based on the sea-viewing wide field-of-view sensor (SeaWiFS) approach [26,27], which estimates aerosol reflectance in VIS wavelengths from two NIR bands with iterative optimization for turbid water [12,28,29]. This process first corrects a priori gaseous absorption transmitted by ozone, nitrogen dioxide, and water vapor. Spectral response functions of general ocean-color sensors including GOCI-II are designed to avoid the water vapor absorption spectral range [30]. However, this spectrum crosses the out-of-band response range of the GOCI-II sensor from the red to NIR bands. Therefore, enhancing the quality of total precipitable water (TPW), which is the total atmospheric water vapor in a vertical column, would contribute considerably to improving atmospheric corrections.

There are two candidate TPW sources for GOCI-II atmospheric correction: National Centers for Environmental Prediction (NCEP) forecast field data and advanced meteorological imager (AMI) TPW data estimated by nine infrared bands from 6.3 to 13.3 um [31]. The NCEP forecast data are currently used for GOCI-II atmospheric correction implemented in the GOCI-II ground segment (G2GS) product because its 3-day advance distribution [32] is ideal for real-time GOCI-II data processing. However, they have lower spatial resolution (0.25°) than the GOCI-II sensor, and may have lower accuracy than real-time observations or reanalysis data [33]. By contrast, the AMI sensor provides full-disk TPW information, including the GOCI-II observation area, with enhanced spatial (6 km) and temporal resolution (10 min). Therefore, the AMI TPW fully covers the spatiotemporal range of GOCI-II

and reflects water vapor absorption effects, providing a high-resolution TPW product similar to that of GOCI-II.

In this study, we consider the gas absorption effect in near real-time by fusing simultaneous GOCI-II and AMI observations, and investigate the possibility of improving the accuracy of GOCI-II atmospheric correction and primary ocean-color products. We evaluated radiosonde observations over the GOCI-II local area and analyzed the effects of different TPW datasets on primary ocean-color products (i.e., R_{rs}, CHL, TSS, and CDOM) using the GOCI-II atmospheric correction integrated with the TPW correction model [34].

2. Data and Method

2.1. GOCI-II Atmospheric Correction (AC) Algorithm

The GOCI-II AC algorithm is an extension of the previous GOCI AC algorithm [12,28,35] with four additional bands centered at 380, 510, 620, and 709 nm. Notably, the 620 and 709 nm bands make it possible to enhance atmospheric correction accuracy for highly turbid water by considering different sediment types using the spectral relationships of inherent optical properties (e.g., absorption and back scattering coefficients) among the 620, 709, 745, and 865 nm bands [36].

The GOCI-II AC retrieves water reflectance at the sea surface (ρ_{wn}) by removing the atmospheric contributions. Ignoring sunglint, whitecaps, and the effects of bidirectional reflectance, the TOA reflectance (ρ_{TOA}) at wavelength λ can be described as follows:

$$\rho_{TOA}(\lambda) = \left(\rho_r(\lambda) + \rho_{am}(\lambda) + t_d^v(\lambda)t_d^s(\lambda)\rho_{wn}(\lambda)\right) \Big/ t_g^v(\lambda)t_g^s(\lambda)', \quad (1)$$

where ρ_{wn} is the reflectance at the sea surface, ρ_r is the Rayleigh reflectance in the absence of aerosols and gaseous absorption, and ρ_{am} is the aerosol multiple-scattering reflectance in the presence of air molecules without gaseous absorption. The terms t_d^v and t_d^s are the diffuse transmittances from the sea surface to the sensor and from the sun to the sea surface, respectively. The upward and downward gaseous transmittance t_g^v and t_g^s is divided into transmittance by ozone ($t_{oz}^{v(s)}$) and water vapor ($t_{wv}^{v(s)}$) as follows:

$$t_g^{v(s)}(\lambda) = t_{oz}^{v(s)}(\lambda)\, t_{wv}^{v(s)}(\lambda), \quad (2)$$

From Equation (1), the Rayleigh reflectance can be precisely (<1% error) computed by radiative transfer simulations for given geometric angles, air pressure, and wind speed. The ρ_{am} for VIS wavelengths can be estimated from that for the two NIR bands (i.e., 745 and 865 nm) [28] based on the black-pixel assumption [36]. For gaseous absorption, $t_{oz}^{v(s)}$ can be estimated based on the Beer–Lambert Law. The water vapor transmittance ($t_{wv}^{v(s)}$), which is discussed in detail below, was described by Lee et al. [34]. The transmittance model was established through linear regression using radiative transfer simulation data [37] based on an assumed single water vapor vertical profile [38]. Simulation data were generated for solar zenith angles of 0–80°, viewing zenith angles of 0–80°, air pressure of 657.54–1013 mb, and TPW of 0–10 g/cm^2. Then, the $t_{wv}^{v(s)}$ model considering air pressure is derived as follows:

$$\mathrm{t}_{wv} = \ln\left(a_0 NSCD^3 + a_1 NSCD^2 + a_2 NSCD\right), \quad (3)$$

with

$$a_i = b_0 + \sum_{j=0}^{3} b_{ij} \times \left(\frac{press}{1013}\right)^j \quad (4)$$

where NSCD is the normalized slant column density, calculated as $\left({}^{\mathrm{TPW}}/_{\cos\theta}\right) \div c_N$, in which c_N is the normalization value (=57.5877) and *press* is the atmospheric pressure at sea level. The values of regression coefficients a and b are listed in Table 1.

Table 1. Regression coefficients for the estimation of water vapor transmittance [34].

Band (Wavelength)	Coefficient	b0	b1	b2	b3
7 (620 nm)	a1	−0.10883	0.15571	−0.07120	0.00984
	a2	0.16363	−0.14028	0.00169	0.01588
	a3	0.07286	−0.46455	0.40572	−0.10403
	a4	−0.00074	0.00121	−0.00062	2.71837
8 (660 nm)	a1	0.45515	−2.36725	2.27751	−0.62727
	a2	−1.18466	5.04707	−4.51584	1.18857
	a3	1.23797	−4.13265	3.13151	−0.73864
	a4	−0.01231	0.01268	−0.00183	2.71741
9 (680 nm)	a1	−0.00710	0.01315	−0.00761	0.00131
	a2	0.01882	−0.02768	0.01214	−0.00122
	a3	0.00810	−0.08087	0.07458	−0.01982
	a4	−0.00025	0.00066	−0.00057	2.71845
10 (709 nm)	a1	−2.31743	3.25378	−1.44822	0.18822
	a2	2.79502	−1.88244	−0.59034	0.46462
	a3	1.37638	−6.47705	5.51278	−1.40445
	a4	−0.02817	0.05269	−0.03369	2.72560
11 (745 nm)	a1	−0.40148	−0.84316	1.42884	−0.47871
	a2	−0.11748	3.58159	−4.02118	1.18320
	a3	1.36350	−5.09311	4.14129	−1.02827
	a4	−0.02499	0.04092	−0.02223	2.72225
12 (865 nm)	a1	−1.25817	1.61226	−0.57056	0.02898
	a2	1.35500	−0.46605	−0.85665	0.40739
	a3	0.74989	−3.53807	3.05438	−0.78668
	a4	−0.02085	0.04073	−0.02682	2.72422

2.2. Data

2.2.1. GOCI-II Data

GOCI-II has two observation modes, full-disk and local area [39]. In full-disk mode, the hemispherical sphere (latitude, 81.18°S to 71.21°N; longitude, 46.92°E to 150.01°W) is divided into 235 slots, and one observation per day is provided for each slot. In local area mode, 10 daytime hourly images are collected from 8:15 to 17:15 Korea Standard Time (KST) by dividing the Northeast Asian Sea (2500 × 2500 km^2 centered at 36°N, 130°E) into 12 slots (Figure 1) [22]. The study area corresponds to slot index 7 (Figure 1, orange shading), which includes the Korean peninsula, with various ranges of ocean optical characteristics from 24 May to 31 December 2021.

GOCI-II has 12 spectral bands, including 1 near-ultraviolet (UV) band (380 nm), 8 VIS bands (412, 443, 490, 510, 555, 620, 660, and 680 nm), and 3 NIR bands (709, 745, and 865 nm) for ocean environmental monitoring (Table 2). Radiances were measured according to six bands from red to NIR (bands 7–12) that are directly affected by water vapor absorption in the path of solar radiation. The remaining bands (bands 1–6) are not affected by water vapor absorption. However, because both NIR channels (745 and 865 nm) are used for aerosol correction in the GOCI-II atmospheric correction algorithm, water vapor absorption can affect R_{rs} for all GOCI-II bands. Therefore, in this study, we used 11 GOCI-II bands (bands 2–12) to evaluate GOCI-II water vapor absorption correction improvement. The first spectral band (380 nm) was excluded due to its considerable photo-response nonuniformity.

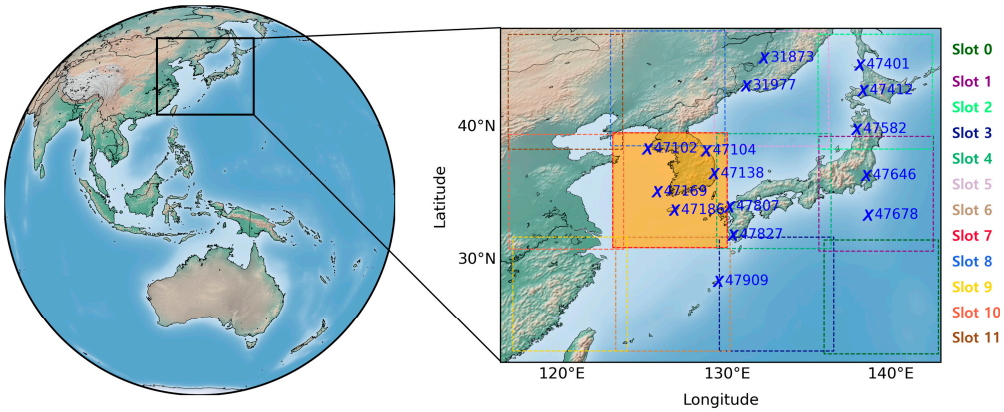


Figure 1. The observation area of geostationary ocean color imager (GOCI-II) (**left**) full-disk and (**right**) local area mode. The observation area of each slot (dashed boxes) for local area mode is overlaid on a background image of the Korean peninsula. Radiosonde observation locations are indicated by blue "X" symbol. Orange shading indicates the observation area of slot 7.

Table 2. GOCI-II spectral specifications. The number in parentheses means the water vapor transmittance for an air pressure of 1013 mb, total precipitable water (TPW) of 3 g/cm^2, and zenith angle of 30°.

Band	Central Wavelength (nm)	Bandwidth (nm)	Water Vapor Absorption
1	380	20	X
2	412	20	X
3	440	20	X
4	490	20	X
5	512	20	X
6	555	20	X
7	620	20	O (0.9961)
8	660	20	O (0.9816)
9	680	10	O (0.9993)
10	709	10	O (0.9635)
11	745	20	O (0.9723)
12	865	40	O (0.9951)

2.2.2. AMI and NCEP TPW Data

The AMI onboard the Geo-Kompsat 2 (GK-2A) satellite has been in operation since December 2018 [23] in the same geostationary orbit as GOCI-II (128.2°E). It provides more than 52 products, including TPW for monitoring land, atmosphere, and ocean environments over the Asia and Oceania region every 10 min. The 6 km resolution TPW product is generated by the AMI atmospheric profile (AAP) algorithm using nine infrared (IR) bands ranging from 6300 to 13,300 nm, with an optimal estimation method based on inversion [40]. GK-2A TPW was validated using 1095 Vaisala RS92 radiosonde observations; the results showed good accuracy, with a root mean square error (RMSE) of 2.82 mm and correlation coefficient (R) of 0.98 [31].

NCEP generates numerous atmospheric and land products, including temperature, wind field, precipitation, and soil moisture data through the global forecast system (GFS), which couples atmosphere, ocean, land, and sea-ice models to accurately simulate weather conditions [32]. The forecast data used in this study was generated from GFS v16, in which the number of vertical layers was increased to 127 and the top layer was extended from the upper stratosphere to the mesopause. We used hourly 0.25° Spatial resolution data available from NCEP (https://nomads.ncep.noaa.gov/pub/data/nccf/com/gfs/prod/, accessed on 2 February 2023).

The GOCI-II AC algorithm uses air pressure, ozone concentration, wind field, and TPW data provided by NCEP as ancillary input [41]; their temporal and spatial ranges are the same as those of the GOCI-II data. We also used AMI TPW as a substitute for NCEP TPW to consider near-real-time and high-resolution water vapor information in gas absorption correction, and analyze its impact on primary ocean-color products.

Both AMI and NCEP data are spatially interpolated using the bicubic method to match the spatial resolution of GOCI-II (0.25 km). For AMI TPW data, we used 20 min of data per hour. For NCEP TPW data, hourly data were used to consider the GOCI-II slot 7 observation time (27 min per hour).

2.2.3. Rawinsonde Measurements

To evaluate AMI and NCEP TPW data, we used radiosonde observations provided by the University of Wyoming. These data comprise 13 parameters including atmospheric pressure, temperature, wind speed, and mixing ratio data for each altitude level every 12 h (00:00 and 12:00 Zulu time). TPW can be calculated according to the mixing ratio of each pressure level using Equation (1).

$$\mathrm{TPW} = \frac{1}{\tau g} \int mx \, dp, \tag{5}$$

where τ and g are the density of water and acceleration due to gravity, respectively, and mx is the mixing ratio at pressure p. TPW data based on radiosonde observations were used as reference data to assess the accuracy of satellite-based TPW products [40,42]. Because only a few stations are represented in slot 7, we used data from 15 stations within the GOCI-II local observation area, which may be downloaded from the Wyoming University website (http://weather.uwyo.edu/upperair/sounding.html, accessed on 9 June 2022). The locations of these stations are indicated in Figure 1.

2.3. Methods

To evaluate the quality of ocean-color products R_{rs}, CDOM, TSS, and CHL according to TPW products, we validated the AMI and NCEP TPW products, retrieved ocean-color products, and performed uncertainty analysis. These steps are described in detail in the following sections.

2.3.1. Validation of AMI and NCEP TPW Products in the GOCI-II Observation Area

To evaluate uncertainties in ocean-color products caused by TPW variability, we assessed the accuracy of AMI and NCEP TPW data through comparison with radiosonde observations. We used radiosonde observation data for only 00:00 Zulu time, which is included in the GOCI-II observation window. Then, we matched 15 radiosonde observation stations to the nearest pixels of interpolated AMI and NCEP TPW data; finally, 3725 data were used for validation. Accuracy was evaluated in terms of RMSE, R, and mean absolute percentage error (MAPE), which are widely utilized to quantify the accuracy of continuous remotely sensed variables [43]. These metrics are mathematically expressed as follows:

$$\mathrm{MAPE} = \frac{100}{n} \sum_{i=1}^{n} \left| \frac{ref_i - est_i}{ref_i} \right|, \tag{6}$$

$$\mathrm{RMSE} = \sqrt{\frac{\sum_{i=1}^{n} (ref_i - est_i)^2}{n}}, \tag{7}$$

$$\mathrm{R} = \frac{\sum_{i=1}^{n} \left(ref_i - \overline{ref_i} \right) \left(est_i - \overline{est_i} \right)}{\sqrt{\sum_{i=1}^{n} \left(ref_i - \overline{ref_i} \right)^2} \sqrt{\sum_{i=1}^{n} \left(est_i - \overline{est_i} \right)^2}}, \tag{8}$$

where n means number of matchups; ref_i and est_i are ith reference and estimation value, respectively; and $\overline{ref_i}$ and $\overline{est_i}$ are averages of ref_i and est_i, respectively.

Among their metrics, MAPE was considered uncertain on AMI and NCEP TPW and used in uncertainty estimation. The details are described in Section 2.3.3.

2.3.2. Primary Ocean-Color Products

To analyze the sensitivity of the four primary ocean-color products (R_{rs}, CHL, TSS, and CDOM) to variation in TPW, the products were generated through G2GS operational algorithms using AMI and NCEP TPW data as input, and then compared.

To analyze the primary products, we used remote-sensing reflectance (R_{rs}) instead of ρ_{wn} because it is used more widely for ocean-color algorithms. R_{rs} is calculated as follows:

$$R_{rs} = \Re \frac{F}{\pi} \rho_{wn}, \tag{9}$$

where $\Re$ is the bidirectional effect correction function for the Fresnel transmittance at the air–ocean interface and F is the bidirectional effect correction factor by the scattering phase function of in-water particles.

The GOCI-II CDOM algorithm estimates absorption coefficients for a blue wavelength, e.g., 440 nm ($a_{dom}440$). At blue wavelengths, where absorption by CDOM is strong, TSS and CHL also strongly absorb solar radiation. Thus, the GOCI-II CDOM algorithm uses the ratio of R_{rs} at 490 and 555 nm in addition to R_{rs} at 443 nm. This algorithm is based on the Yellow Sea Large Marine Ecosystem Ocean-color Work Group (YOC) algorithm [44] and was modified for GOCI-II [45] as follows:

$$a_{dom}440 = 10^{a_0 + a_1 log_{10} R + a_2 log_{10} R^2}, \tag{10}$$

$$R = \left(\frac{R_{rs}(490\ nm)}{R_{rs}(555\ nm)} \right) R_{rs}(443\ nm)^{0.059}, \tag{11}$$

where, $a_{0,1,2}$ are coefficients for $a_{dom}440$ retrieval (= −1.23, −2.311, and −2.16, respectively).

The GOCI-II TSS algorithm (Equation (11)) retrieves concentrations of materials suspended at the sea surface using the weighted sum of TSSs estimated by the YOC and switching algorithms. The switching algorithm uses R_{rs} at 620 and 709 nm, which were newly added in GOCI-II. These bands are appropriate for TSS retrieval for turbid water, but may not be suitable for clear water due to their low signal-to-noise ratios. Therefore, the YOC algorithm was improved to increase reliability of the algorithm for both low and high turbidity, as follows:

$$TSS = (1 - \omega_{YOC}) TSS_{SWITCH} + \omega_{YOC} TSS_{YOC} \tag{12}$$

where TSS_{YOC} and TSS_{SWITCH} are derived by YOC and switching algorithm, respectively. The weighting coefficients ω_{YOC} calculated as $\frac{7 - TSS_{YOC}}{7 - 1}$.

The switching algorithm first calculates TSS for low (TSS_{LOW}) and high turbidity (TSS_{HIGH}) using R_{rs} at 620 and 709 nm, respectively (Equations (13) and (14)), considering saturation effects. Then, both TSSs are combined using a weight (ω_{LT}) that represents turbidity, which is determined using R_{rs} at 620 nm (Equation (15)), i.e., $[0.0245 - R_{rs}\ (620\ \text{nm})]/[0.0245 - 0.017]$, as follows:

$$TSS_{LOW} = l_0 + l_1 R_{rs}620 + l_2 R_{rs}620^2 + l_3 R_{rs}620^3, \tag{13}$$

$$TSS_{HIGH} = h_0 + h_1 R_{rs}709 + h_2 R_{rs}709^2 + h_3 R_{rs}709^3, \tag{14}$$

$$TSS_{SWITCH} = \omega_{LT} TSS_{LOW} + (1 - \omega_{LT}) TSS_{HIGH}, \tag{15}$$

where coefficients l and h are defined as $l_{0,1,2,3}$ = [1.067 × 10^3, −8.36 × 10^4, 5.95 × 10^6, −1.88 × 10^7] and $h_{0,1,2,3}$ = [3.19 × 10^1, −1.10 × 10^3, −7.73 × 10^3, 9.64 × 10^6], respectively. TSS_{SWITCH} is the result of switching algorithm.

The YOC algorithm was based on Siswanto et al. [44] and has a form similar to that of the CDOM algorithm; it uses R_{rs} for three bands (490, 555, and 660 nm) and its coefficients were modified for GOCI-II as follows:

$$TSS_{YOC} = 10^{c_0 + c_1(R_{rs}555 + R_{rs}660) + c_2(R_{rs}490/R_{rs}555)} \quad (16)$$

where TSS_{YOC} is the result of the YOC algorithm. $c_{0,1,2}$ are coefficients optimized for GOCI-II (0.649, 25.623, and −0.646, respectively).

The GOCI-II CHL algorithm estimates the concentration of chlorophyll-a based on the difference in absorption between its blue and green wavelengths [46,47]. The GOCI-II CHL algorithm adapts the ocean chlorophyll 4-band (OC4S) algorithm, which includes the maximum band ratio as follows:

$$log_{10}CHL = \sum_{i=0}^{4} b_i \left(log_{10} \left(\frac{Max(R_{rs}443,\ R_{rs}490,\ R_{rs}510)}{R_{rs}555} \right) \right)^i, \quad (17)$$

where coefficients $b_{0,1,2,3,4}$ [0.3272, –2.994, 2.7218, –1.2259, –0.5683] are currently used in the SeaWiFS CHL algorithm [48].

2.3.3. Uncertainty Analysis

TPW correction affects aerosol reflectance correction by altering the TOA radiance of two NIR bands (745 and 865 nm). Thus, inaccurate TPW data may cause uncertainty in all ocean-color products, including R_{rs}, CDOM, TSS, and CHL. Moreover, a poor understanding of this uncertainty can introduce significant errors in subsequent applications and may influence the inferred conclusions [49]. In this study, we estimated uncertainty in ocean-color products due to TPW error based on the law of uncertainty propagation proposed in a previous study [50], as follows:

$$u_{OC} = \sqrt{\left(\frac{\partial_{OC}}{\partial_{TPW}} \right)^2 u_{TPW}^2} \quad (18)$$

where u_{OC} is the standard uncertainty of ocean-color products, $\frac{\partial_{OC}}{\partial_{TPW}}$ is the sensitivity coefficient of ocean-color products related to TPW, and u_{TPW} is the uncertainty in TPW, based on the MAPE of AMI and NCEP TPW evaluated using radiosonde observations.

3. Results

3.1. Validation of NCEP and AMI TPW

Prior to evaluating the uncertainty of ocean-color products associated with TPW error, we assessed the accuracy of the AMI and NCEP TPW data. Figure 2 presents a scatter plot of AMI and NCEP TPW data and radiosonde observations, and Figure 3 shows the trends in RMSE and MAPE of AMI and NCEP TPW over time, and for each station. Both validation results indicate that the AMI data had a consistently higher accuracy than the NCEP data in terms of R, RMSE, and MAPE.

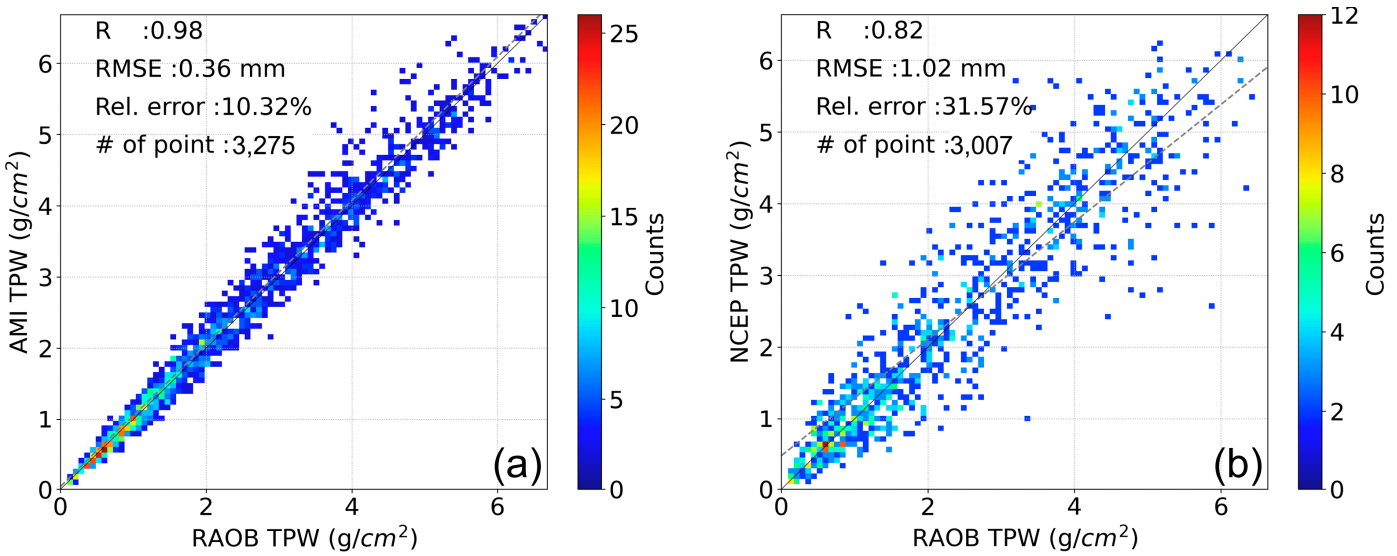


Figure 2. Scatter plot of radiosonde total precipitable water (TPW) observations, and (**a**) advanced meteorological imager (AMI) and (**b**) National Centers for Environmental Prediction (NCEP) TPW data. Color gradient indicates the number of data points in 0.065 × 0.065 bins. Rel. error refers to mean absolute percentage error. Solid and dash lines indicate the 1:1 line and regression line, respectively. "# of point" means the number of data.

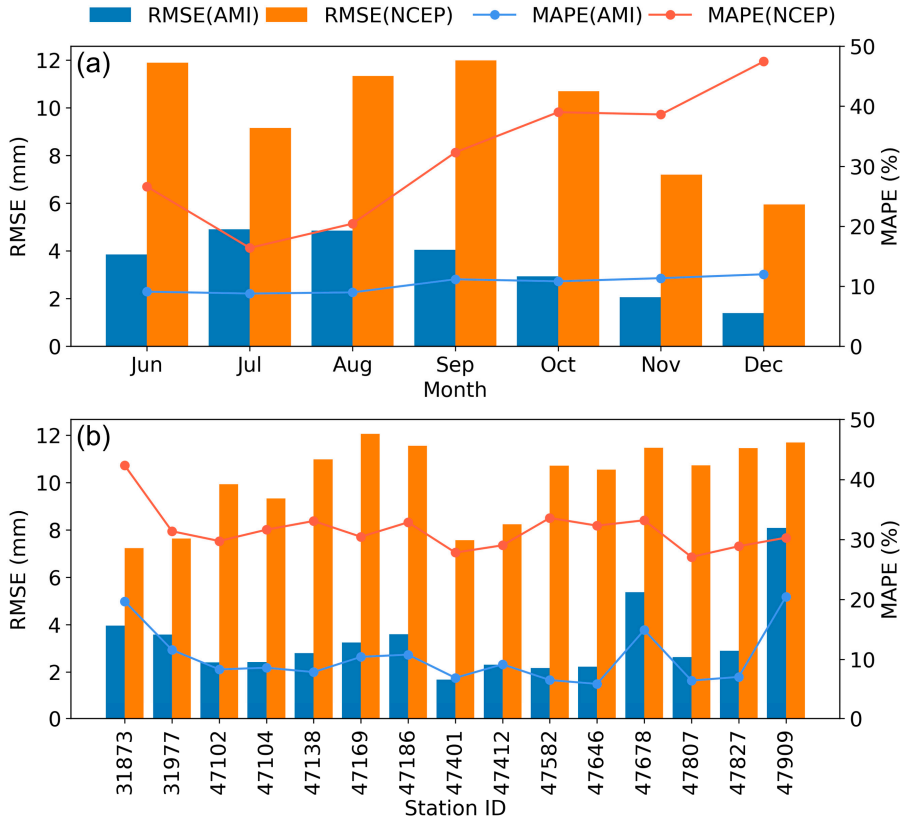


Figure 3. Validation results for AMI and NCEP TPW compared to radiosonde observations according to (**a**) month and (**b**) station identification number. May were excluded due to lack of data.

As shown in Figure 2, AMI TPW data had a higher R (0.98) and lower error (RMSE = 3.65 mm; MAPE = 10.32%) than NCEP TPW (R = 0.85; RMSE = 10.2 mm; MAPE = 31.57%). This result is consistent with that of a previous study [29]. AMI TPW also had more stable MAPE over time (8.79–12.0%) than NCEP TPW (16.60–47.45%) (Figure 3a).

The RMSE of AMI TPW tended to increase slightly during summer (June–August), which is the rainy season in the Korean peninsula, whereas RMSE of NCEP TPW did not reflect seasonal patterns.

The MAPEs of AMI and NCEP TPW showed similar patterns among stations; however, AMI TPW had a significantly lower error than NCEP TPW at all stations (Figure 3b). This indicates that AMI TPW had a lower error and better represented the spatiotemporal variability of TPW than NCEP TPW. Therefore, using AMI TPW as input data for the G2GS AC algorithm would provide more accurate water vapor absorption correction than using NCEP TPW, leading to improved spatiotemporal consistency in ocean-color products.

3.2. Effects of Different TPW Data on Atmospheric Correction

The strength of water vapor absorption increased in the order 709, 745, 660, 620, 865, and 680 nm; however, its inter-band effects in atmospheric correction were complex because each band affected each other band during both aerosol and turbidity correction. This section presents the results of a case analysis to analyze the effects of different TPWs on ocean-color products.

Figure 4 shows the differences between NCEP and AMI TPW (NCEP TPW–AMI TPW), ρ_{rc}, and R_{rs} at 03:15 UTC on 11 September 2021. The TPW difference ranged from –1.26 to 1.53 g/cm^2 (Figure 4a). At 745 nm, the difference in ρ_{rc} ranged from –0.00082 to 0.00069 (Figure 4b), and that of R_{rs} at 412 nm ranged from –0.00960 to 0.00878 (Figure 4c) despite the lack of a water vapor absorption effect in this band. The spatial pattern of the R_{rs} difference at 412 nm was similar, but inversely proportional to that of TPW.

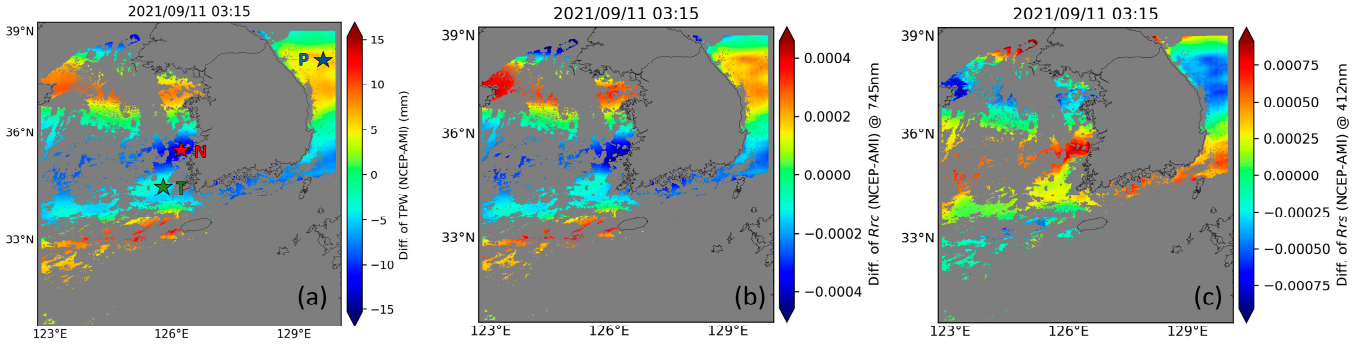


Figure 4. Differences in (**a**) TPW, (**b**) Rayleigh-corrected reflectance at 745 nm, and (**c**) remote sensing reflectance at 412 nm obtained using different TPW sources (NCEP and AMI) at 03:15 UTC on 11 September 2021. Gray shading indicates masked regions corresponding to land, cloud cover, and beyond the slot. "T" and "N" represent pixels with positive and negative differences in TPW (NCEP–AMI) in clear water, respectively, while "P" represents a pixel in turbid water.

This mechanism can be explained in terms of the three reflectances of atmospheric correction: ρ_{rc}, aerosol reflectance and R_{rs}. Figure 5 shows the atmospheric correction results for the three reflectance cases obtained using different TPW sources, indicated in Figure 4a as points N (clear water; TSS = 0.025 g/m^3, TPW difference = –0.90 g/cm^2), P (clear water; TSS = 0.007 g/m^3, TPW difference = 0.70 g/cm^2), and T (turbid water; TSS = 14.84 g/m^3, TPW difference = –0.41 g/cm^2). At point N, the slope between two ρ_{rc} values at 745 and 865 nm decreased when NCEP TPW was used (Figure 5a) due to the black-pixel assumption, which led to an underestimation of the aerosol reflectance towards shorter wavelengths (7.71%, 7.27%, 6.51%, 6.31%, and 5.31% for 412, 443, 490, 512, and 555 nm, respectively) (Figure 5b). This underestimation of aerosol reflectance caused an overestimation of R_{rs}, which exceeded the GOCI-II spectral range under the fixed total reflectance budget (46.71%, 18.30%, 11.76%, 13.34%, and 13.69% for 412, 443, 490, 12, and 555 nm, respectively) (Figure 5c). By contrast, at point P, the slope between two ρ_{rc} values at 745 and 865 nm increased when NCEP TPW was used, which led to an overestimation of the aerosol reflectance across the entire spectral range and an underestimation of R_{rs}

(Figure 5). As with point N, at point T, the slope between the two ρ_{rc} values at 745 and 865 nm decreased due to a negative TPW difference, which induced a smaller increment of aerosol reflectance toward shorter wavelengths, thereby underestimating the aerosol reflectance in the VIS bands, although aerosol reflectance at the two NIR bands was high through the iterative process of separating aerosol and water reflectance in turbid water. Thus, R_{rs} was overestimated in the NIR bands and underestimated in the VIS bands. However, relative differences in the VIS bands (3.30%, 1.88%, 0.97%, 0.86%, and 0.52% for 412, 443, 490, 12, and 555 nm, respectively) were smaller than those for the clear water case (point N) due to the high VIS R_{rs} in turbid water.

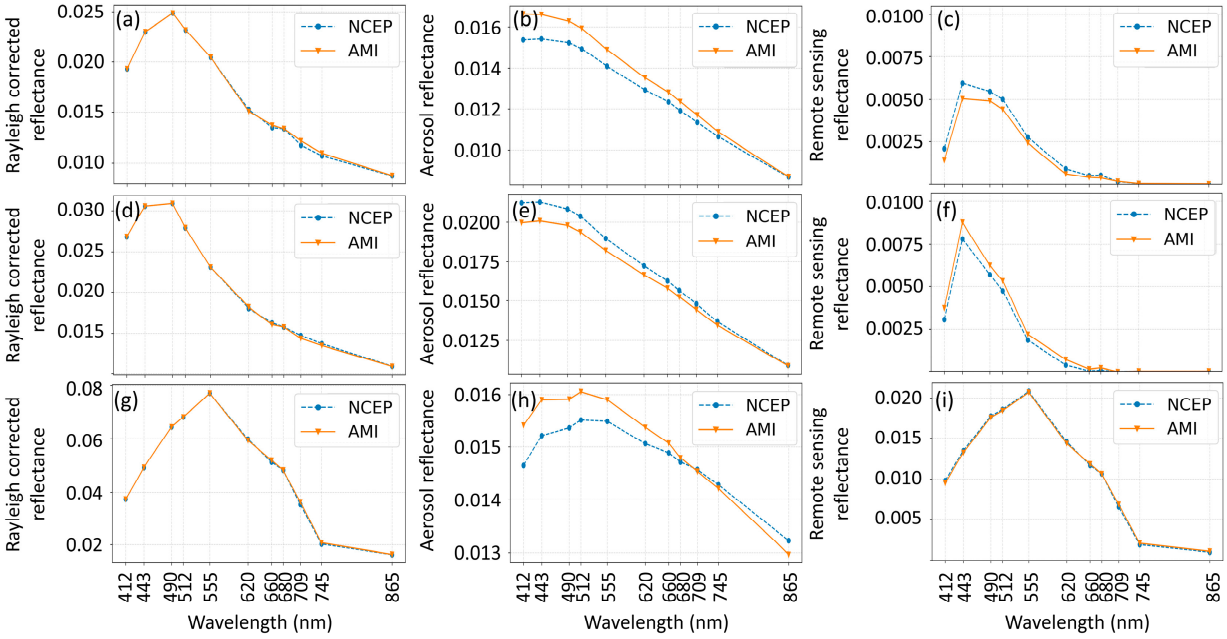


Figure 5. Spectral profiles of (**left**) Rayleigh-corrected reflectance, (**center**) aerosol reflectance, and (**right**) remote sensing reflectance for sample pixels (**a**–**c**) N, (**d**–**f**) P, and (**g**–**i**) T, which are indicated by stars in Figure 4. Solid orange and blue dashed lines are results obtained using AMI and NCEP TPW data, respectively.

3.3. Effects of Different TPW Sources on Primary Ocean-Color Products

This section presents differences and uncertainty in ocean-color products due to different TPW data sources. Figure 6 shows an overall comparison of R_{rs} values calculated using NCEP and AMI data for 11 GOCI-II bands used in this study. Although all bands indicate a negligible bias (<0.00005), the points were evenly scattered around the 1:1 line. This trend was more pronounced at shorter wavelengths due to the aerosol reflectance estimation from the ρ_{rc} of the two NIR bands. The TPW difference produced different aerosol reflectance estimates and had a more significant effect at shorter wavelengths [51]. For example, in the blue and green bands, which had a center wavelength of 412–555 nm (Figure 4), MAPEs ranged from 2.97 to 6.43%. The MAPE for R_{rs} (412 nm) was larger than the global climate observing system (GCOS) requirement of <5% for blue and green wavelengths. Therefore, accurate, high-resolution ancillary data are required for climate research in the ocean-color remote sensing field. The higher MAPE values in the red and NIR bands (Figure 6) were related to their low magnitude [52].

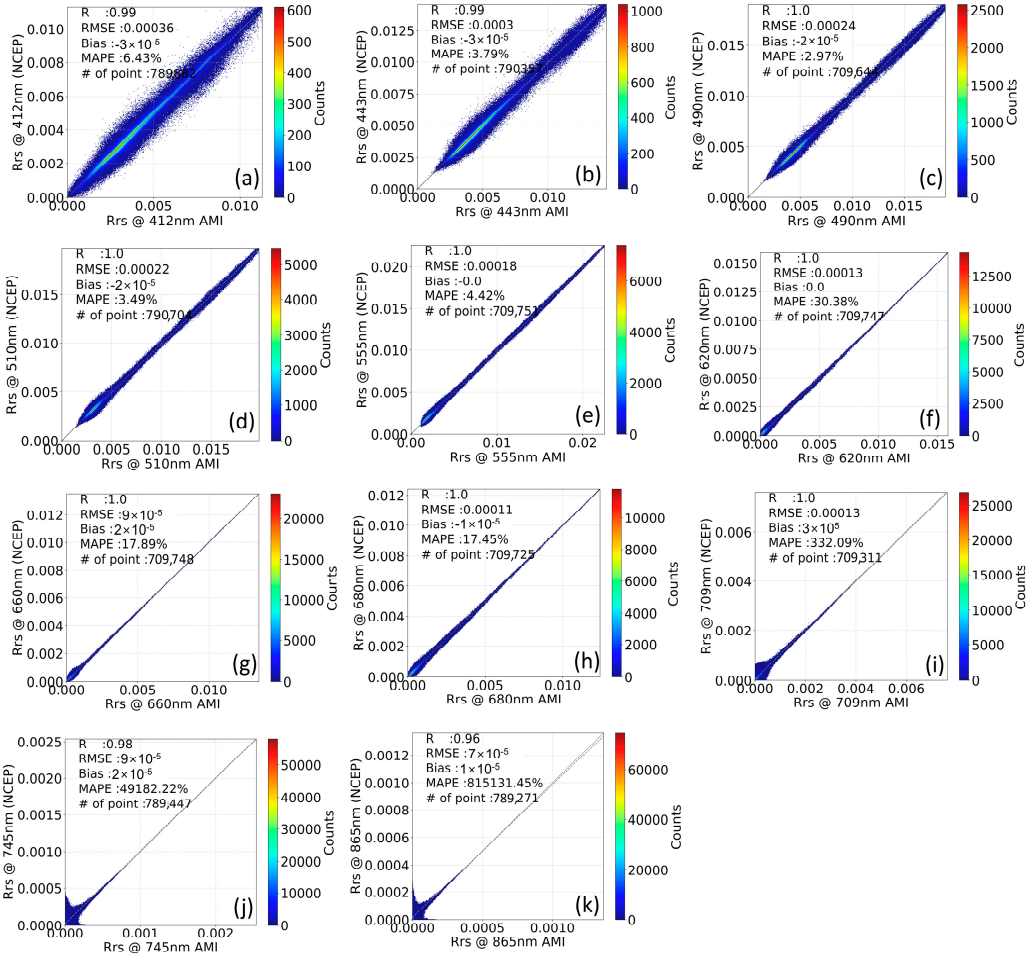


Figure 6. Scatter plots of remote sensing reflectances for (**a**) 412, (**b**) 443, (**c**) 490, (**d**) 510, (**e**) 555, (**f**) 620, (**g**) 660, (**h**) 680, (**i**) 709, (**j**) 745, and (**k**) 865 nm. Solid and dashed lines in each figure indicate the 1:1 and regression lines, respectively.

Comparisons of the other three ocean-color products (CHL, CDOM, and TSS) yielded similar results to the R_{rs} comparison, with a low bias and slight scattering of data points (Figure 7). The MAPE values for CHL, CDOM, and TSS were 3.53%, 6.18%, and 7.71%, respectively. These results indicate that, unlike R_{rs}, the TPW difference did not significantly affect the CHL, CDOM, and TSS ocean-color products, as the required accuracy of CHL suggested by GCOS is 30%. The band ratio used in this study for the CHL, CDOM, and TSS retrieval algorithm had only a small effect on aerosol reflectance difference caused by TPW differences. However, in the morning and evening, when the path was longer, the water vapor absorption uncertainty caused by TPW differences became more extensive. Therefore, as shown in Figure 8, the MAPE of three ocean-color products tended to increase at higher solar zenith angles, such that MAPE at 17:00 KST was more than double that at noon, increasing from 3.24%, 5.43%, and 6.77% to 6.63%, 13.53%, and 16.14% for CHL, CDOM, and TSS, respectively. These results imply that inaccurate TPW can represent a significant error factor in analyzing diurnal ocean variation, which is among the most critical roles of a geostationary ocean-color sensor, by degrading the temporal stability of ocean-color products.

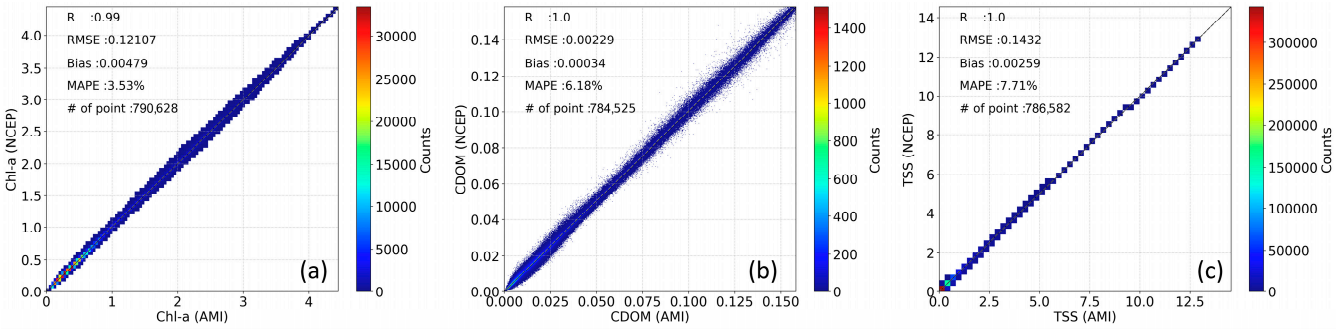


Figure 7. Same with Figure 6 but for ocean-color product: (**a**) chlorophyll-a concentration, (**b**) colored dissolved organic matter, (**c**) total suspended sediment.

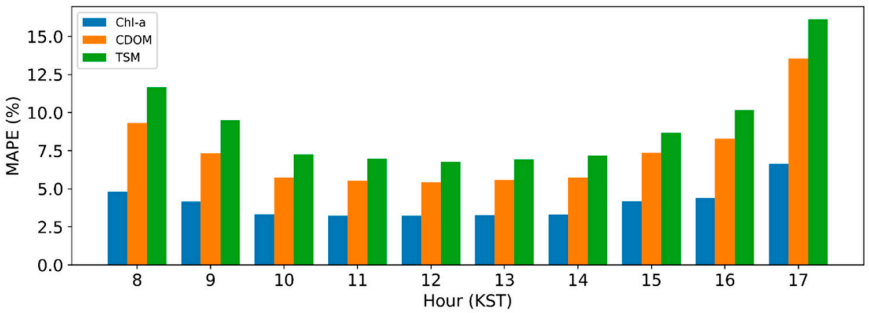


Figure 8. Hourly MAPE of ocean-color products. Blue, orange, and green bars indicate chlorophyll-a, colored dissolved organic matter, and total suspended sediment, respectively.

Table 3 shows the statistical uncertainties of ocean-color products associated with NCEP and AMI TPW, estimated using Equation (18). In this analysis, the uncertainty of NCEP and AMI TPW was set to 1.031 and 3.16 g/cm^2 based on the TPW validation results (Figure 2). These uncertainties show that shorter wavelengths were associated with higher values in the blue and green channels (412–555 nm). Although the error value for the NIR region was very low, relative error increased due to the small signal. This finding is consistent with the previous results of this study. Generally, the NCEP TPW caused an approximately 3-fold higher uncertainty than the AMI TPW. In particular, NCEP TPW generated a nonnegligible uncertainty of 13.15% in R_{rs} at 412 nm. By contrast, AMI TPW generated less uncertainty than the required accuracy of GCOS of 5% in the blue and green channels (2.07%, 1.43%, 1.00%, 0.99%, and 0.84% for 412, 443, 490, 512, and 555 nm, respectively). This indicates that AMI TPW is more suitable for use in GOCI-II atmospheric correction due to its reliability. For CHL, CDOM, and TSS, acceptable uncertainties were obtained by both AMI (CHL, 1.10%; CDOM, 0.96%; TSS, 0.81%) and NCEP (CHL, 3.18%; CDOM, 2.81%; TSS, 2.40%). As briefly mentioned above, this result was related to the band ratio used by these retrieval algorithms.

Table 3. Comparison of estimated uncertainty values for ocean-color products obtained using advanced meteorological imager (AMI) and National Centers for Environmental Prediction (NCEP) TPW data.

Parameter	Uncertainty (AMI)	Uncertainty (NCEP)	Parameter	Uncertainty (AMI)	Uncertainty (NCEP)
R_{rs} (412 nm)	0.00016 sr^{-1} (2.07%)	0.00047 sr^{-1} (6.18%)	R_{rs} (680 nm)	4.40×10^{-5} sr^{-1} (1.71%)	0.00013 sr^{-1} (5.17%)
R_{rs} (443 nm)	0.00013 sr^{-1} (1.43%)	0.00040 sr^{-1} (4.27%)	R_{rs} (709 nm)	2.57×10^{-5} sr^{-1} (2.22%)	8.35×10^{-5} sr^{-1} (6.75%)

Table 3. *Cont.*

Parameter	Uncertainty (AMI)	Uncertainty (NCEP)	Parameter	Uncertainty (AMI)	Uncertainty (NCEP)
R_{rs} (490 nm)	0.00010 sr^{-1} (1.00%)	0.00031 sr^{-1} (3.00%)	R_{rs} (745 nm)	1.35×10^{-5} sr^{-1} (4.18%)	4.08×10^{-5} sr^{-1} (12.61%)
R_{rs} (512 nm)	9.71×10^{-5} sr^{-1} (0.99%)	0.00029 sr^{-1} (2.99%)	R_{rs} (865 nm)	8.17×10^{-6} sr^{-1} (4.81%)	2.47×10^{-5} sr^{-1} (14.54%)
R_{rs} (555 nm)	7.41×10^{-5} sr^{-1} (0.84%)	0.00022 sr^{-1} (2.52%)	CHL	0.01422 mg/m^3 (1.10%)	0.04116 mg/m^3 (3.18%)
R_{rs} (620 nm)	8.33×10^{-5} sr^{-1} (2.02%)	0.00025 sr^{-1} (6.14%)	CDOM	0.00065 m^{-1} (0.96%)	0.00191 m^{-1} (2.81%)
R_{rs} (660 nm)	2.28×10^{-5} sr^{-1} (0.82%)	6.83×10^{-5} sr^{-1} (2.44%)	TSS	0.01918 g/m^3 (0.81%)	0.05721 g/m^3 (2.40%)

4. Discussion

In this study, we improved the accuracy of water vapor absorption correction for GOCI-II by fusing it with GK-2A/AMI data. We also demonstrated its impact on primary ocean-color products through comparative results. The approach we presented can be applied when the ocean-color sensor and the meteorological sensor are operated simultaneously, as in the case of GK-2 satellites. Thus, we anticipate our approach to apply to the United States' next-generation geostationary satellite geosynchronous littoral imaging and monitoring radiometer through fusion with tropospheric emissions: Monitoring of Pollution and Geostationary Operational Environmental Satellites and Geostationary Operational Environmental Satellite series. However, it is necessary to develop a new water vapor transmittance model suitable for specific sensors prior to applying the approach, due to the high sensitivity of water vapor absorption to the sensor's spectral response function.

Unlike previous studies, the water vapor transmittance model used in this study additionally considers the pressure at the sea surface. However, for a robust water vapor transmittance model, it is necessary to address the variability of water vapor profile, which is one of the major challenges in water vapor absorption correction. Figure 9 represents the seasonal variability of water vapor profiles (The data used in this figure were acquired in 2022 at the 15 points shown in Figure 1.) Water vapor profiles exhibit significant temporal variability, particularly in the lower layer of the atmosphere, which can alter water vapor transmittance. An increase in water vapor concentration in the lower atmosphere typically decreases water vapor transmittance due to the effect of multiple scattering. In addition, the interaction between water vapor and aerosol, changes of spectral response function by band aging, and non-uniformity of spectral response can also impact water vapor transmittance. Therefore, these factors might be considered to enhance the water vapor transmittance model.

While our uncertainty analysis demonstrated that utilizing AMI TPW for GOCI-II atmospheric correction reduced uncertainty in the examined primary ocean-color products, we did not compare or validate the results using in situ measurements. Therefore, future studies should verify the accuracy of the approach by conducting validation with a sufficient number of in situ measurements for various atmospheric conditions.

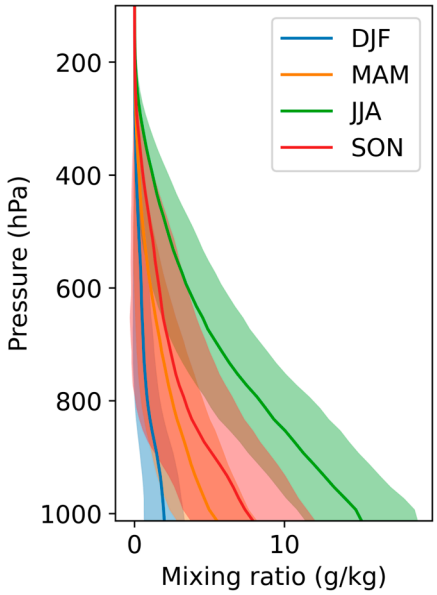


Figure 9. Seasonal (solid line) average and (shade) standard deviation of water vapor profiles for 15 stations in 2022 (DJF: Dec.-Jan.-Feb., MAM: Mar.-Apr.-May, JJA: Jun.-Jul.-Aug., SON: Sep.-Oct.-Nov).

5. Summary and Conclusions

Atmospheric water vapor in Northeast Asia exhibits strong temporal and spatial variability due to seasonal surges of monsoon flow, synoptic-scale pressure systems, and local circulation along its complex coastline and topography. Therefore, inadequate consideration of TPW can cause significant uncertainties in ocean-color products. Given that the GK-2 satellite is equipped with both ocean-color and meteorological sensors, we evaluated the uncertainty of GOCI-II primary ocean-color products using high-resolution AMI TPW instead of the traditional NCEP TPW data in an atmospheric correction algorithm. We found that AMI had higher overall consistency (R = 0.98; MAPE = 10.32%) with radiosonde observations than NCEP (R = 0.85; MAPE = 31.57%; Figure 2). Our validation results indicated that NCEP data did not fully resolve the strong TPW variability (Section 3.1).

High-resolution TPW data can help reduce R_{rs} uncertainties compared to traditional TPW data. In particular, the impact of the AMI TPW data caused a significant difference in ρ_{rc}, particularly at two NIR bands, due to high TPW absorption, which led to variation in aerosol reflectance at the VIS GOCI-II bands. The change in aerosol reflectance impacted R_{rs} in all GOCI-II bands. The relative difference in R_{rs} was more significant in clear water than in turbid water. Generally, the overestimation (underestimation) of TPW led to the underestimation (overestimation) of R_{rs}. The different TPW sources induced negligible biases, but caused nonnegligible MAPEs in R_{rs} at the blue to green bands (412–555 nm), ranging from 2.97% to 6.43%. Notably, the MAPE at 412 nm was more significant than the GCOS requirement, such that inaccurate TPW data may yield R_{rs} data unsuitable for climate studies, even in the absence of other error sources in atmospheric correction.

Replacing TPW input with AMI improved the accuracy of GOCI-II primary ocean-color products. Unlike R_{rs}, CHL, CDOM, and TSS showed nonsignificant overall MAPEs (3.53%, 6.18%, and 7.71%, respectively) based on different TPW sources, considering that the GCOS requirement for CHL is 30%. However, because the improved accuracy of the GOCI-II ocean-color data by AMI TPW depended on the sunlight path length, the application of AMI TPW for GOCI-II ocean-color retrieval may offer advantages in the analysis of diurnal variation [52] and long-term data with spatiotemporal consistency [53].

Our uncertainty analysis showed that NCEP TPW induced an approximately 3-fold higher uncertainty than AMI TPW in primary ocean-color products. NCEP caused a significant error of 13.15% in R_{rs} at 412 nm, whereas the AMI TPW caused uncertainties within 5% in the blue to green bands (2.07%, 1.43%, 1.00%, 0.99%, and 0.84% for 412, 443, 490, 512,

and 555 nm, respectively). Both AMI and NCEP TPW generated acceptable uncertainties for CHL, CDOM, and TSS; however, AMI induced a lower uncertainty than NCEP.

Given the strong variability of water vapor, we demonstrated the possibility of improving the accuracy of data on ocean color by fusing satellite TPW data obtained in the same geostationary orbit. In addition, the effects of other trace gases (e.g., ozone and nitrogen dioxide) on GOCI-II primary ocean-color products should be analyzed using GEMS trace gas products. More realistic considerations of atmospheric gas through a combination of UV, VIS, and IR measurements from various satellites will significantly improve the accuracy of data on ocean color.

Author Contributions: Conceptualization: K.-S.L., M.-S.P. and J.-H.A.; methodology: K.-S.L., M.-S.P. and J.-H.A.; software: K.-S.L. and J.-H.A.; investigation, K.-S.L. and J.-H.A.; writing—original draft preparation, K.-S.L.; writing—review and editing, M.-S.P., J.-H.A. and J.-K.C.; visualization: K.-S.L.; funding acquisition: J.-K.C. All authors have read and agreed to the published version of the manuscript.

Funding: This research was supported by the Korea Institute of Marine Science and Technology Promotion (KIMST) funded by the Ministry of Oceans and Fisheries (20220546).

Data Availability Statement: GOCI-II data are available at the National Ocean Satellite Center website at http://www.nosc.go.kr (accessed on 21 February 2023). The GK-2A/AMI data can be downloaded from National Meteorological Satellite Center website at https://nmsc.kma.go.kr (accessed on 21 February 2023). The NCEP data are available at the NCEP Products Inventory at https://www.nco.ncep.noaa.gov/pmb/products/gfs/ (accessed on 2 February 2023). Rawinsonde measurements data can be downloaded from Wyoming Weather Web at https://weather.uwyo.edu/upperair/sounding.html (accessed on 23 February 2023).

Acknowledgments: The authors would like to thank the National Ocean Satellite Center, National Meteorological Satellite Center, and Wyoming Weather Web for kindly providing the data. In addition, a very special acknowledgement is made to the editors and referees who provided important comments that improved this paper.

Conflicts of Interest: The authors declare no conflict of interest.

Abbreviations and Symbols

AC	Atmospheric correction
AMI	Advanced meteorological imager
CDOM	Colored dissolved organic matter
CHL	Chlorophyll-a concentration
g	Acceleration due to gravity
G2GS	GOCI-II ground segment
GCOS	Global climate observing system
GEMS	Geostationary environmental monitor spectrometer
GFS	Global forecast system
GK-2	Geo-Kompsat-2
GOCI	Geostationary ocean-color imager
GOCI-II	Second geostationary ocean-color imager
IR	Infra-red
KST	Korea standard time
MAPE	Mean absolute percentage error
mx	Mixing ratio at specific pressure
NCEP	National Centers for Environmental Prediction
NIR	Near-infrared
OC4S algorithm	Ocean chlorophyll 4-band algorithm
RMSE	Root mean square error

SeaWiFS	Sea-viewing wide field-of-view sensor
TOA	Top-of-atmosphere
TPW	Total precipitable water
TSS	Total suspended sediment
UTC	Universal time coordinated
UV	Ultraviolet
VIS	Visible
YOC	Yellow Sea Large Marine Ecosystem Ocean-color Work Group
τ	The density of water
R_{rs}	Remote sensing reflectance
ρ_{wn}	Water reflectance at the sea surface
ρ_{TOA}	TOA reflectance
ρ_r	Rayleigh reflectance in the absence of aerosols and gaseous absorption
ρ_{am}	Aerosol multiple-scattering reflectance in the presence of air molecules without gaseous absorption
t_d^v	Diffuse transmittances from the sea surface to the sensor
t_d^s	Diffuse transmittances from the sun to the sea surface
t_g^v	The upward gaseous transmittance
t_g^s	The downward gaseous transmittance
$t_{oz}^{v(s)}$	The upward (downward) transmittance by ozone
$t_{wv}^{v(s)}$	The upward (downward) transmittance by water vapor
$NSCD$	Normalized slant column density
$press$	The atmospheric pressure at sea level
R	Correlation coefficient
ref_i	i-th reference value
est_i	i-th estimation value
$\Re$	Bidirectional effect correction function for the Fresnel transmittance at the air–ocean interface
F	The light scattering direction of in-water particles
TSS_{YOC}	Total suspended sediments derived by YOC algorithm
TSS_{SWITCH}	Total suspended sediments derived by switching algorithm
TSS_{LOW}	Total suspended solids for low turbidity
TSS_{HIGH}	Total suspended solids for high turbidity
u_{OC}	Standard uncertainty of ocean-color products
$\frac{\partial_{OC}}{\partial_{TPW}}$	Sensitivity coefficient of ocean-color products related to TPW
u_{TPW}	Uncertainty in TPW data

References

1. Kravitz, J.; Matthews, M.; Bernard, S.; Griffith, D. Application of Sentinel 3 OLCI for chl-a retrieval over small inland water targets: Successes and challenges. *Remote Sens. Environ.* **2019**, *237*, 111562. [CrossRef]
2. Park, M.-S.; Lee, S.; Ahn, J.-H.; Lee, S.-J.; Choi, J.-K.; Ryu, J.-H. Decadal Measurements of the First Geostationary Ocean Color Satellite (GOCI) Compared with MODIS and VIIRS Data. *Remote Sens.* **2021**, *14*, 72. [CrossRef]
3. Kim, W.; Moon, J.-E.; Park, Y.-J.; Ishizaka, J. Evaluation of chlorophyll retrievals from Geostationary Ocean Color Imager (GOCI) for the North-East Asian region. *Remote Sens. Environ.* **2016**, *184*, 482–495. [CrossRef]
4. Tan, X.; Sun, B.; Wang, G.; Cheng, T.; Huang, K.; Shen, F. Consecutive retrieval of aerosol optical depth and total suspended solid concentration in turbid coastal water of Eastern China. *J. Quant. Spectrosc. Radiat. Transf.* **2022**, *287*, 108231. [CrossRef]
5. Doxaran, D.; Lamquin, N.; Park, Y.-J.; Mazeran, C.; Ryu, J.-H.; Wang, M.; Poteau, A. Retrieval of the seawater reflectance for suspended solids monitoring in the East China Sea using MODIS, MERIS and GOCI satellite data. *Remote Sens. Environ.* **2013**, *146*, 36–48. [CrossRef]
6. Wei, J.; Wang, M.; Jiang, L.; Yu, X.; Mikelsons, K.; Shen, F. Global Estimation of Suspended Particulate Matter from Satellite Ocean Color Imagery. *J. Geophys. Res. Oceans* **2021**, *126*, e2021JC017303. [CrossRef]
7. Cao, F.; Miller, W.L. A new algorithm to retrieve chromophoric dissolved organic matter (CDOM) absorption spectra in the UV from ocean color. *J. Geophys. Res. Oceans* **2015**, *120*, 496–516. [CrossRef]
8. Wang, Y.; Shen, F.; Sokoletsky, L.; Sun, X. Validation and Calibration of QAA Algorithm for CDOM Absorption Retrieval in the Changjiang (Yangtze) Estuarine and Coastal Waters. *Remote Sens.* **2017**, *9*, 1192. [CrossRef]

9. Al-Kharusi, E.S.; Tenenbaum, D.E.; Abdi, A.M.; Kutser, T.; Karlsson, J.; Bergström, A.K.; Berggren, M. Large-Scale Retrieval of Coloured Dissolved Organic Matter in Northern Lakes Using Sentinel-2 Data. *Remote Sens.* **2020**, *12*, 157. [CrossRef]
10. Frouin, R.J.; Franz, B.A.; Ibrahim, A.; Knobelspiesse, K.; Ahmad, Z.; Cairns, B.; Chowdhary, J.; Dierssen, H.M.; Tan, J.; Dubovik, O.; et al. Atmospheric Correction of Satellite Ocean-Color Imagery during the PACE Era. *Front. Earth Sci.* **2019**, *7*, 145. [CrossRef]
11. Melin, F.; Colandrea, P.; De Vis, P.; Hunt, S.E. Sensitivity of Ocean Color Atmospheric Correction to Uncertainties in Ancillary Data: A Global Analysis with SeaWiFS Data. *IEEE Trans. Geosci. Remote Sens.* **2022**, *60*, 1–18. [CrossRef]
12. Ahn, J.-H.; Park, Y.-J.; Ryu, J.-H.; Lee, B.; Oh, I.S. Development of atmospheric correction algorithm for Geostationary Ocean Color Imager (GOCI). *Ocean Sci. J.* **2012**, *47*, 247–259. [CrossRef]
13. Wang, M. A Sensitivity Study of the SeaWiFS Atmospheric Correction Algorithm Effects of Spectral Band Variations. *Remote Sens. Environ.* **1999**, *67*, 348–359. [CrossRef]
14. Gordon, H.R. Evolution of Ocean Color Atmospheric Correction: 1970–2005. *Remote Sens.* **2021**, *13*, 5051. [CrossRef]
15. Mograne, M.A.; Jamet, C.; Loisel, H.; Vantrepotte, V.; Mériaux, X.; Cauvin, A. Evaluation of Five Atmospheric Correction Algorithms over French Optically-Complex Waters for the Sentinel-3A OLCI Ocean Color Sensor. *Remote Sens.* **2019**, *11*, 668. [CrossRef]
16. Wang, M.; Franz, B. Comparing the ocean color measurements between MOS and SeaWiFS: A vicarious intercalibration approach for MOS. *IEEE Trans. Geosci. Remote Sens.* **2000**, *38*, 184–197. [CrossRef]
17. Gordon, H.; Voss, K. *MODIS Normalized Water-Leaving Radiance Algorithm Theoretical Basis Document (MOD 18)*, 5th ed.; NASA: Washington, DC, USA, 2004.
18. Ramachandran, S.; Wang, M. Near-Real-Time Ocean Color Data Processing Using Ancillary Data from the Global Forecast System Model. *IEEE Trans. Geosci. Remote Sens.* **2010**, *49*, 1485–1495. [CrossRef]
19. Tzortziou, M.; Parker, O.; Lamb, B.; Herman, J.R.; Lamsal, L.; Stauffer, R.; Abuhassan, N. Atmospheric Trace Gas (NO_2 and O_3) Variability in South Korean Coastal Waters, and Implications for Remote Sensing of Coastal Ocean Color Dynamics. *Remote Sens.* **2018**, *10*, 1587. [CrossRef]
20. Tzortziou, M.; Herman, J.R.; Ahmad, Z.; Loughner, C.P.; Abuhassan, N.; Cede, A. Atmospheric NO_2 dynamics and impact on ocean color retrievals in urban nearshore regions. *J. Geophys. Res. Oceans* **2014**, *119*, 3834–3854. [CrossRef]
21. Ahmad, Z.; McClain, C.R.; Herman, J.R.; Franz, B.A.; Kwiatkowska, E.J.; Robinson, W.D.; Bucsela, E.J.; Tzortziou, M. Atmospheric correction for NO_2 absorption in retrieving water-leaving reflectances from the SeaWiFS and MODIS measurements. *Appl. Opt.* **2007**, *46*, 6504. [CrossRef]
22. Lee, S.J.; Lee, K.S.; Han, T.H.; Moon, J.E.; Bae, S.; Choi, J.K. Introduction on the products and the quality management plans for GOCI-II. *Korean J. Remote Sens.* **2021**, *37*, 1245–1257.
23. Lee, K.-S.; Chung, S.-R.; Lee, C.; Seo, M.; Choi, S.; Seong, N.-H.; Jin, D.; Kang, M.; Yeom, J.-M.; Roujean, J.-L.; et al. Development of Land Surface Albedo Algorithm for the GK-2A/AMI Instrument. *Remote Sens.* **2020**, *12*, 2500. [CrossRef]
24. Choi, W.J.; Moon, K.J.; Yoon, J.; Cho, A.; Kim, S.; Lee, S.; Ko, D.H.; Kim, J.; Ahn, M.H.; Kim, D.R.; et al. Introducing the Geostationary Environment Monitoring Spectrometer. *J. Appl. Rem. Sens.* **2018**, *12*, 0044005. [CrossRef]
25. Choi, J.K.; Park, M.S.; Han, K.S.; Kim, H.C.; Im, J. One year of GOCI-II launch present and future. *Korean J. Remote Sens.* **2021**, *37*, 1229–1234.
26. Wang, M.; Gordon, H.R. A simple, moderately accurate, atmospheric correction algorithm for SeaWiFS. *Remote Sens. Environ.* **1994**, *50*, 231–239. [CrossRef]
27. Bailey, S.W.; Franz, B.A.; Werdell, P.J. Estimation of near-infrared water-leaving reflectance for satellite ocean color data processing. *Opt. Express* **2010**, *18*, 7521–7527. [CrossRef]
28. Ahn, J.-H.; Park, Y.-J.; Kim, W.; Lee, B. Simple aerosol correction technique based on the spectral relationships of the aerosol multiple-scattering reflectances for atmospheric correction over the oceans. *Opt. Express* **2016**, *24*, 29659–29669. [CrossRef]
29. Ahn, J.-H.; Park, Y.-J.; Fukushima, H. Comparison of Aerosol Reflectance Correction Schemes Using Two Near-Infrared Wavelengths for Ocean Color Data Processing. *Remote Sens.* **2018**, *10*, 1791. [CrossRef]
30. Fan, Y.; Li, W.; Chen, N.; Ahn, J.-H.; Park, Y.-J.; Kratzer, S.; Schroeder, T.; Ishizaka, J.; Chang, R.; Stamnes, K. OC-SMART: A machine learning based data analysis platform for satellite ocean color sensors. *Remote Sens. Environ.* **2020**, *253*, 112236. [CrossRef]
31. National Meteorological Satellite Center Home Page. Available online: https://nmsc.kma.go.kr/homepage/html/base/cmm/selectPage.do?page=static.edu.atbdGk2a (accessed on 10 August 2022).
32. NCEP. GFS Website. Available online: https://www.emc.ncep.noaa.gov/emc/pages/numerical_forecast_systems/gfs.php (accessed on 11 August 2022).
33. Jabbari, A.; Bae, D.-H. Application of Artificial Neural Networks for Accuracy Enhancements of Real-Time Flood Forecasting in the Imjin Basin. *Water* **2018**, *10*, 1626. [CrossRef]
34. Lee, K.S.; Ahn, J.H.; Park, M.S. GOCI-II Capability of Improving the Accuracy of Ocean Color Products through Fusion with GK-2A/AMI. *Korean J. Remote Sens.* **2021**, *37*, 1295–1305.
35. Ahn, J.-H.; Park, Y.-J.; Kim, W.; Lee, B.; Oh, I.S. Vicarious calibration of the Geostationary Ocean Color Imager. *Opt. Express* **2015**, *23*, 23236–23258. [CrossRef]
36. Ahn, J.-H.; Park, Y.-J. Estimating Water Reflectance at Near-Infrared Wavelengths for Turbid Water Atmospheric Correction: A Preliminary Study for GOCI-II. *Remote Sens.* **2020**, *12*, 3791. [CrossRef]

37. Vermote, E.F.; Tanré, D.; Deuze, J.L.; Herman, M.; Morcette, J.-J. Second Simulation of the Satellite Signal in the Solar Spectrum, 6S: An overview. *IEEE Trans. Geosci. Remote Sens.* **1997**, *35*, 675–686. [CrossRef]
38. United States Committee on Extension to the Standard Atmosphere. *U.S. Standard Atmosphere 1976*; U.S. Government Printing Office: Washington, DC, USA, 1976.
39. National Ocean Color Satellite Center Homepage. Available online: https://www.nosc.go.kr/eng/ (accessed on 6 February 2023).
40. Lee, S.J.; Ahn, M.-H.; Chung, S.-R. Atmospheric Profile Retrieval Algorithm for Next Generation Geostationary Satellite of Korea and Its Application to the Advanced Himawari Imager. *Remote Sens.* **2017**, *9*, 1294. [CrossRef]
41. GOCI-II Atmospheric Correction Algorithm Theoretical Basis Document. Available online: https://www.nosc.go.kr/eng/board/actionBoardViewBoard0011.do?SEARCH_CODE=&SEARCH_WORD=&SEARCH_CATEGORY=&BOARD_SNO=20&boardSelectPage=1 (accessed on 7 February 2023).
42. Zhang, Y.; Li, J.; Li, Z.; Zheng, J.; Wu, D.; Zhao, H. FENGYUN-4A advanced geosynchronous radiation imager layered precipitable water vapor products' comprehensive evaluation based on quality control system. *Atmosphere* **2022**, *13*, 290. [CrossRef]
43. Loew, A.; Bell, W.; Brocca, L.; Bulgin, C.E.; Burdanowitz, J.; Calbet, X.; Donner, R.V.; Ghent, D.; Gruber, A.; Kaminski, T.; et al. Validation practices for satellite-based Earth observation data across communities. *Rev. Geophys.* **2017**, *55*, 779–817. [CrossRef]
44. Siswanto, E.; Tang, J.; Yamaguchi, H.; Yuhwan, A.; Ishizaka, J.; Yoo, S.; Sangwoo, K.; Kiyomoto, Y.; Yamada, K.; Chiang, C.; et al. Empirical ocean-color algorithms to retrieve chlorophyll-a, total suspended matter, and colored dissolved or-ganic matter absorption coefficient in the Yellow and East China Seas. *J. Oceanogr.* **2011**, *67*, 627–650. [CrossRef]
45. GOCI-II Absorption of Colored Dissolved Organic Matter Theoretical Basis Document. Available online: https://www.nosc.go.kr/eng/board/actionBoardViewBoard0011.do?SEARCH_CODE=&SEARCH_WORD=&SEARCH_CATEGORY=&BOARD_SNO=15&boardSelectPage=1 (accessed on 7 February 2023).
46. Liu, G.; Lin, L.; Song, K.; Li, Y.; Lyu, H.; Wen, Z.; Fang, C.; Bi, S.; Sun, X.; Wang, Z.; et al. An OLCI-based algorithm for semi-empirically partitioning absorption coefficient and estimating chlorophyll a concentration in various turbid case-2 waters. *Remote Sens. Environ.* **2020**, *239*, 111648. [CrossRef]
47. O'Reilly, J.E.; Werdell, P.J. Chlorophyll algorithms for ocean color sensors—OC4, OC5 & OC6. *Remote Sens. Environ.* **2019**, *229*, 32–47.
48. NASA. NASA Ocean Color. Available online: https://oceancolor.gsfc.nasa.gov/atbd/chlor_a/#sec_2 (accessed on 23 April 2020).
49. Shuai, Y.; Tuerhanjiang, L.; Shao, C.; Gao, F.; Zhou, Y.; Xie, D.; Liu, T.; Liang, J.; Chu, N. Re-understanding of land surface albedo and related terms in satellite-based retrievals. *Big Earth Data* **2020**, *4*, 45–67. [CrossRef]
50. *ENV 13005: 2008*; Guide to the Expression of Uncertainty in Measurement. ISO: Geneva, Switzerland, 2008.
51. Kim, W.; Moon, J.-E.; Ahn, J.-H.; Park, Y.-J. Evaluation of Stray Light Correction for GOCI Remote Sensing Reflectance Using in Situ Measurements. *Remote Sens.* **2016**, *8*, 378. [CrossRef]
52. Concha, J.; Mannino, A.; Franz, B.; Kim, W. Uncertainties in the Geostationary Ocean Color Imager (GOCI) Remote Sensing Reflectance for Assessing Diurnal Variability of Biogeochemical Processes. *Remote Sens.* **2019**, *11*, 295. [CrossRef]
53. Van Oostende, M.; Hieronymi, M.; Krasemann, H.; Baschek, B.; Röttgers, R. Correction of inter-mission inconsistencies in merged ocean colour satellite data. *Front. Remote Sens.* **2022**, *3*, 882418. [CrossRef]

Disclaimer/Publisher's Note: The statements, opinions and data contained in all publications are solely those of the individual author(s) and contributor(s) and not of MDPI and/or the editor(s). MDPI and/or the editor(s) disclaim responsibility for any injury to people or property resulting from any ideas, methods, instructions or products referred to in the content.